

1

2 Modular strategies for spatial mapping of 3 multi-modal mouse brain data

4 Nicholas J. Tustison¹, Min Chen², Fae N. Kronman³, Jeffrey T. Duda², Clare Gamlin⁴, Mia
5 G. Tustison, Michael Kunst⁴, Rachel Dalley⁴, Staci Sorenson⁴, Quanxin Wang⁴, Lydia Ng⁴,
6 Yongsoo Kim³, and James C. Gee²

7 ¹Department of Radiology and Medical Imaging, University of Virginia, Charlottesville, VA

8 ²Department of Radiology, University of Pennsylvania, Philadelphia, PA

9 ³Department of Neural and Behavioral Sciences, Penn State University, Hershey, PA

10 ⁴Allen Institute for Brain Science, Seattle, WA

11

12 Corresponding authors:

13

14 Nicholas J. Tustison, DSc

15 Department of Radiology and Medical Imaging

16 University of Virginia

17 ntustison@virginia.edu

18

19 James C. Gee, PhD

20 Department of Radiology

21 University of Pennsylvania

22 gee@upenn.edu

²³ **Abstract**

²⁴ Large-scale efforts by the BRAIN Initiative Cell Census Network (BICCN) are generating a
²⁵ comprehensive reference atlas of cell types in the mouse brain. A key challenge in this effort
²⁶ is mapping diverse datasets—acquired with varied imaging, tissue processing, and profiling
²⁷ methods—into shared coordinate frameworks. Here, we present modular mapping pipelines
²⁸ developed using the Advanced Normalization Tools Ecosystem (ANTsX) to align MERFISH
²⁹ spatial transcriptomics and high-resolution fMOST morphology data to the Allen Common
³⁰ Coordinate Framework (CCFv3), and developmental MRI and LSFN data to the Devel-
³¹ opmental CCF (DevCCF). Simultaneously, we introduce two novel methods: 1) a velocity
³² field-based approach for continuous interpolation across developmental timepoints, and 2)
³³ a deep learning framework for automated brain parcellation using minimally annotated and
³⁴ publicly available data. All workflows are open-source and reproducible. We also provide
³⁵ general guidance for selecting appropriate strategies across modalities, enabling researchers
³⁶ to adapt these tools to new data.

³⁷ 1 Introduction

³⁸ Over the past decade, there have been significant advancements in mesoscopic single-cell analysis of the mouse brain. It is now possible to track single neurons¹, observe whole-brain developmental changes at cellular resolution², associate brain regions with genetic composition³, and locally characterize neural connectivity⁴. These scientific achievements have been propelled by high-resolution profiling and imaging techniques that enable submicron, multimodal, three-dimensional characterizations of whole mouse brains. Among these are micro-optical sectioning tomography^{5,6}, tissue clearing methods^{1,7}, spatial transcriptomics^{8,9}, and single-cell genomic profiling¹⁰, each offering expanded specificity and resolution for cell-level brain analysis.

⁴⁷ Recent efforts by the NIH BRAIN Initiative have mobilized large-scale international collaborations to create a comprehensive reference database of mouse brain structure and function. ⁴⁹ The BRAIN Initiative Cell Census Network has aggregated over 40 multimodal datasets from ⁵⁰ more than 30 research groups¹¹, many of which are registered to standardized anatomical coordinate systems to support integrated analysis. Among the most widely used of these frameworks is the Allen Mouse Brain Common Coordinate Framework (CCFv3)¹². Other CCFs ⁵³ include modality-specific references^{13–15} and developmental atlases^{16,17} that track structural change across time.

⁵⁵ 1.1 Mouse brain mapping challenges

⁵⁶ Robust mapping of cell type data into CCFs is essential for integrative analysis of morphology, ⁵⁷ connectivity, and molecular identity. However, each modality poses unique challenges. For ⁵⁸ example, differences in tissue processing, imaging protocols, and anatomical completeness ⁵⁹ often introduce artifacts such as distortion, tearing, holes, and signal dropout^{18–23}. Intensity ⁶⁰ differences and partial representations of anatomy can further complicate alignment. Given ⁶¹ this diversity specialized strategies are often needed to address the unique, modality-specific ⁶² challenges.

⁶³ Existing mapping solutions fall into three broad categories. The first includes integrated

64 processing platforms that provide users with mapped datasets (e.g., Allen Brain Cell
65 Atlas²⁴, Brain Architecture Portal²⁵, OpenBrainMap²⁶, and Image and Multi-Morphology
66 Pipeline²⁷). These offer convenience and high-quality curated data, but limited gener-
67 alizability and customization. The second category involves highly specialized pipelines
68 tailored to specific modalities such as histology^{28–30}, magnetic resonance imaging (MRI)^{31–33},
69 microCT^{34,35}, light sheet fluorescence microscopy (LSFM)^{36,37}, fluorescence micro-optical
70 sectioning tomography (fMOST)^{15,38}, and spatial transcriptomics, including multiplexed
71 error-robust fluorescence in situ hybridization (MERFISH)^{39–41}. While effective, these
72 solutions often require extensive engineering effort to adapt to new datasets or modalities.
73 Finally, general-purpose toolkits such as elastix⁴², Slicer3D⁴³, and the Advanced Normaliza-
74 tion Tools Ecosystem (ANTsX)⁴⁴ have all been applied to mouse brain mapping scenarios
75 (e.g.,⁴⁵). These toolkits support modular workflows that can be flexibly composed from
76 reusable components, offering a powerful alternative to rigid, modality-specific solutions.
77 However, their use often requires familiarity with pipeline modules, parameter tuning, and
78 tool-specific conventions which can limit adoption.

79 Building on this third category, we describe a set of modular, ANTsX-based pipelines specif-
80 ically tailored for mapping diverse mouse brain data into standardized anatomical frame-
81 works. These include two new pipelines: a velocity field-based interpolation model that
82 potentially enables biologically plausible transformations across developmental timepoints,
83 and a template-based deep learning pipeline for brain extraction and parcellation requiring
84 minimal annotated data. In addition, we include two modular pipelines for aligning multi-
85 plexed error-robust fluorescence in situ hybridization (MERFISH) and fMOST datasets to
86 the Allen CCFv3. These workflows were adapted and tailored using ANTsX tools to support
87 collaborative efforts within the BICCN and are now made openly available in a reproducible
88 format. To facilitate broader adoption, we also provide general guidance for customizing
89 these strategies across imaging modalities and data types. We first introduce key compo-
90 nents of the ANTsX toolkit, which provide a basis for all of the mapping workflows described
91 here, and then detail the specific contributions made in each pipeline.

92 **1.2 The Advanced Normalization Tools Ecosystem (ANTsX)**

93 The Advanced Normalization Tools Ecosystem (ANTsX) has been used in a number of
94 applications for mapping mouse brain data as part of core processing steps in various
95 workflows^{30,46–49}, particularly its pairwise, intensity-based image registration capabilities⁵⁰
96 and bias field correction⁵¹. Historically, ANTsX development is based on foundational ap-
97 proaches to image mapping^{52–54}, especially in the human brain, with key contributions such
98 as the Symmetric Normalization (SyN) algorithm⁵⁰. It has been independently evaluated
99 in diverse imaging domains including multi-site brain MRI⁵⁵, pulmonary CT⁵⁶, and multi-
100 modal brain tumor registration⁵⁷.

101 Beyond registration, ANTsX provides functionality for template generation⁵⁸, intensity-based
102 segmentation⁵⁹, preprocessing^{51,60}, and deep learning⁴⁴. It has demonstrated strong perfor-
103 mance in consensus labeling⁶¹, brain tumor segmentation⁶², and cardiac motion estimation⁶³.
104 Built on the Insight Toolkit (ITK)⁶⁴, ANTsX benefits from open-source contributions while
105 supporting continued algorithm evaluation and innovation. In the context of mouse brain
106 data, ANTsX provides a robust platform for developing modular pipelines to map diverse
107 imaging modalities into CCFs. This paper highlights its use across distinct BICCN projects
108 such as spatial transcriptomic data from MERFISH, structural data from fMOST, and mul-
109 timodal developmental data from LSFM and MRI. We describe both shared infrastructure
110 and targeted strategies adapted to the specific challenges of each modality.

111 **1.3 Novel ANTsX-based open-source contributions**

112 We introduce two novel contributions to ANTsX developed as part of collabortive efforts
113 in creating the Developmental Common Coordinate Framework (DevCCF)¹⁶. First, we
114 present an open-source velocity field-based interpolation framework for continuous map-
115 ping across the sampled embryonic and postnatal stages of the DevCCF atlas¹⁶. This
116 functionality enables biologically plausible interpolation between timepoints via a time-
117 parameterized diffeomorphic velocity model⁶⁵, inspired by previous work⁶⁶. Second, we
118 present a deep learning pipeline for structural parcellation of the mouse brain from mul-

¹¹⁹ timodal MRI data. This includes two novel components: 1) a template-derived brain ex-
¹²⁰ traction model using augmented data from two ANTsX-derived template datasets^{67,68}, and
¹²¹ 2) a template-derived parcellation model trained on DevCCF P56 labelings mapped from
¹²² the AllenCCFv3. This pipeline demonstrates how ANTsX tools and public resources can be
¹²³ leveraged to build robust anatomical segmentation pipelines with minimal annotated data.
¹²⁴ We independently evaluate this framework using a longitudinal external dataset⁶⁹, demon-
¹²⁵ strating generalizability across specimens and imaging protocols. All components are openly
¹²⁶ available through the R and Python ANTsX packages, with general-purpose functionality
¹²⁷ documented in a reproducible, cross-platform tutorial (<https://tinyurl.com/antsxtutorial>).
¹²⁸ Code specific to this manuscript, including scripts to reproduce the novel contributions
¹²⁹ and all associated evaluations, is provided in a dedicated repository (<https://github.com/>
¹³⁰ [ntustison/ANTsXMouseBrainMapping](https://github.com/ntustison/ANTsXMouseBrainMapping)). Additional tools for mapping spatial transcriptomic
¹³¹ (MERFISH) and structural (fMOST) data to the AllenCCFv3 are separately available at
¹³² (<https://github.com/dontminchenit/CCFAlignmentToolkit>).

133 **2 Results**

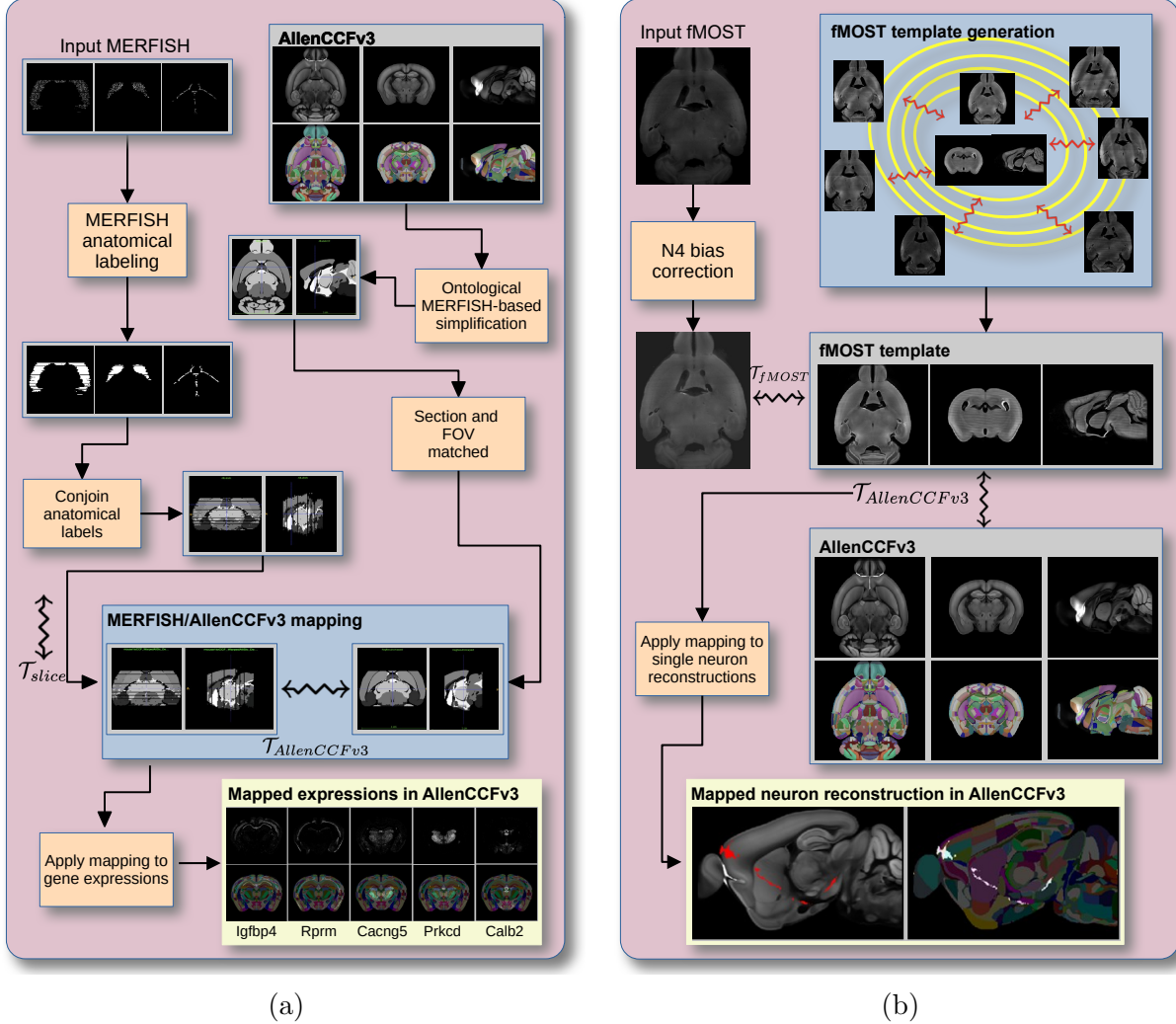


Figure 1: Diagram of the two ANTsX-based pipelines for mapping (a) MERFISH and (b)fMOST data into the space of AllenCCFv3. Each generates the requisite transforms, \mathcal{T} , to map individual images to the CCF.

134 **2.1 AllenCCFv3 brain image mapping**

135 **2.1.1 Mapping multiplexed error-robust fluorescence *in situ* hybridization
136 (MERFISH) data**

137 **Overview.** The ANTsX framework was used to develop a pipeline for mapping multiplexed
138 error-robust fluorescence *in situ* hybridization (MERFISH) spatial transcriptomic mouse

¹³⁹ data onto the AllenCCFv3 (see Figure 1(a)). This pipeline, used recently in creating a
¹⁴⁰ high-resolution transcriptomic atlas of the mouse brain⁴⁹, performs mappings by first gen-
¹⁴¹ erating anatomical labels from tissue related gene expressions in the MERFISH data, and
¹⁴² then spatially matching these labels to corresponding anatomical tissue parcellations in the
¹⁴³ AllenCCFv3. The pipeline consists of MERFISH data specific preprocessing which includes
¹⁴⁴ section reconstruction, mapping corresponding anatomical labels between AllenCCFv3 and
¹⁴⁵ the spatial transcriptomic maps of the MERFISH data, and matching MERFISH sections
¹⁴⁶ to the atlas space. Following preprocessing, two main alignment steps were performed: 1)
¹⁴⁷ 3-D global affine mapping and section matching of the AllenCCFv3 into the MERFISH data
¹⁴⁸ and 2) 2-D global and deformable mapping between each MERFISH section and matched
¹⁴⁹ AllenCCFv3 section. Mappings learned via each step in the pipeline are preserved and con-
¹⁵⁰ catenated to provide point-to-point correspondence between the original MERFISH data
¹⁵¹ and AllenCCFv3, thus allowing individual gene expressions to be transferred into the Al-
¹⁵² lenCCFv3.

¹⁵³ **Data.** MERFISH mouse brain data was acquired using a previously detailed procedure⁴⁹.
¹⁵⁴ Briefly, a brain of C57BL/6 mouse was dissected according to standard procedures and
¹⁵⁵ placed into an optimal cutting temperature (OCT) compound (Sakura FineTek 4583) in
¹⁵⁶ which it was stored at -80°C. The fresh frozen brain was sectioned at 10 μ m on Leica 3050
¹⁵⁷ S cryostats at intervals of 200 μ m to evenly cover the brain. A set of 500 genes were imaged
¹⁵⁸ that had been carefully chosen to distinguish the ~5200 clusters of our existing RNAseq
¹⁵⁹ taxonomy. For staining the tissue with MERFISH probes, a modified version of instructions
¹⁶⁰ provided by the manufacturer was used⁴⁹. Raw MERSCOPE data were decoded using
¹⁶¹ Vizgen software (v231). Cells were segmented based on DAPI and PolyT staining using
¹⁶² Cellpose^{70,71}. Segmentation was performed on a median z-plane (fourth out of seven) and
¹⁶³ cell borders were propagated to z-planes above and below. To assign cluster identity to each
¹⁶⁴ cell in the MERFISH dataset, we mapped the MERFISH cells to the scRNA-seq reference
¹⁶⁵ taxonomy.

¹⁶⁶ **Evaluation.** Alignment of the MERFISH data into the AllenCCFv3 was qualitatively as-
¹⁶⁷ sessed by an expert anatomist at each iteration of the registration using known correspon-

168 dence of gene markers and their associations with the AllenCCFv3. As previously reported⁴⁹,
169 further assessment of the alignment showed that, of the 554 terminal regions (gray matter
170 only) in the AllenCCFv3, only seven small subregions were missed from the MERFISH
171 dataset: frontal pole, layer 1 (FRP1), FRP2/3, FRP5; accessory olfactory bulb, glomerular
172 layer (AOBgl); accessory olfactory bulb, granular layer (AOBgr); accessory olfactory bulb,
173 mitral layer (AOBmi); and accessory supraoptic group (ASO).

174 2.1.2 Mapping fluorescence micro-optical sectioning tomography (fMOST) data

175 **Overview.** We developed a pipeline for mapping fluorescence micro-optical sectioning to-
176 mography (fMOST) mouse brain images into the AllenCCFv3 (see Figure 1(b)). The pipeline
177 is adapted from previously developed frameworks for human brain mapping⁵⁸, and uses a
178 modality specific (fMOST) average atlas to assist in the image registration and mapping.
179 This approach has been well validated in human studies^{72–74}, and successfully used in other
180 mouse data^{12,15,75}. Briefly, we construct an intensity- and shape-based average fMOST atlas
181 using 30 fMOST images to serve as an intermediate registration target for mapping fMOST
182 images from individual specimens into the AllenCCFv3. Preprocessing steps include down-
183 sampling to match the $25\mu m$ isotropic AllenCCFv3, acquisition-based stripe artifact removal,
184 and inhomogeneity correction⁵¹. Preprocessing also includes a single annotation-driven reg-
185 istration to establish a canonical mapping between the fMOST atlas and the AllenCCFv3.
186 This step allows us to align expert determined landmarks to accurately map structures
187 with large morphological differences between the modalities, which are difficult to address
188 using standard approaches. Once this canonical mapping is established, standard intensity-
189 based registration is used to align each new fMOST image to the fMOST specific atlas.
190 This mapping is concatenated with the canonical fMOST atlas-to-AllenCCFv3 mapping to
191 further map each individual brain into the latter without the need to generate additional
192 landmarks. Transformations learned through this mapping can be applied to single neuron
193 reconstructions from the fMOST images to evaluate neuronal distributions across different
194 specimens into the AllenCCFv3 for the purpose of cell census analyses.

195 **Data.** The high-throughput and high-resolution fluorescence micro-optical sectioning to-

¹⁹⁶ mography (fMOST)^{76,77} platform was used to image 55 mouse brains containing gene-defined
¹⁹⁷ neuron populations, with sparse transgenic expression^{78,79}. In short, the fMOST imaging
¹⁹⁸ platform results in 3-D images with voxel sizes of $0.35 \times 0.35 \times 1.0 \mu\text{m}^3$ and is a two-channel
¹⁹⁹ imaging system where the green channel displays the green fluorescent protein (GFP) labeled
²⁰⁰ neuron morphology and the red channel is used to visualize the counterstained propidium
²⁰¹ iodide cytoarchitecture. The spatial normalizations described in this work were performed
²⁰² using the red channel, which offered higher tissue contrast for alignment, although other
²⁰³ approaches are possible including multi-channel registration.

²⁰⁴ **Evaluation.** Evaluation of the canonical fMOST atlas to Allen CCFv3 mapping was per-
²⁰⁵ formed via quantitative comparison at each step of the registration and qualitative assess-
²⁰⁶ ment of structural correspondence after alignment by an expert anatomist. Dice values were
²⁰⁷ generated for the following structures: whole brain, 0.99; fimbria, 0.91; habenular com-
²⁰⁸ missure, 0.63; posterior choroid plexus, 0.93; anterior choroid plexus, 0.96; optic chiasm,
²⁰⁹ 0.77; caudate putamen, 0.97. Similar qualitative assessment was performed for each fMOST
²¹⁰ specimen including the corresponding neuron reconstruction data.

²¹¹ **2.2 Continuously mapping the DevCCF developmental trajectory 212 with a velocity flow model**

²¹³ The DevCCF is an openly accessible resource for the mouse brain research community⁸⁰. It
²¹⁴ consists of multi-modal MRI and LSFM symmetric ANTsX-generated templates⁵⁸ sampling
²¹⁵ the mouse brain developmental trajectory, specifically the embryonic (E) and postnatal (P)
²¹⁶ days E11.5, E13.5, E15.5, E18.5 P4, P14, and P56. Each template space includes structural
²¹⁷ labels defined by a developmental ontology. Its utility is also enhanced by a coordinated
²¹⁸ construction with AllenCCFv3. Although this work represents a significant contribution,
²¹⁹ the gaps between time points potentially limit its applicability which could be addressed
²²⁰ through the development of the ability to map not only between time points but also within
²²¹ and across time points.

²²² To continuously generate transformations between the different stages of the DevCCF atlases,

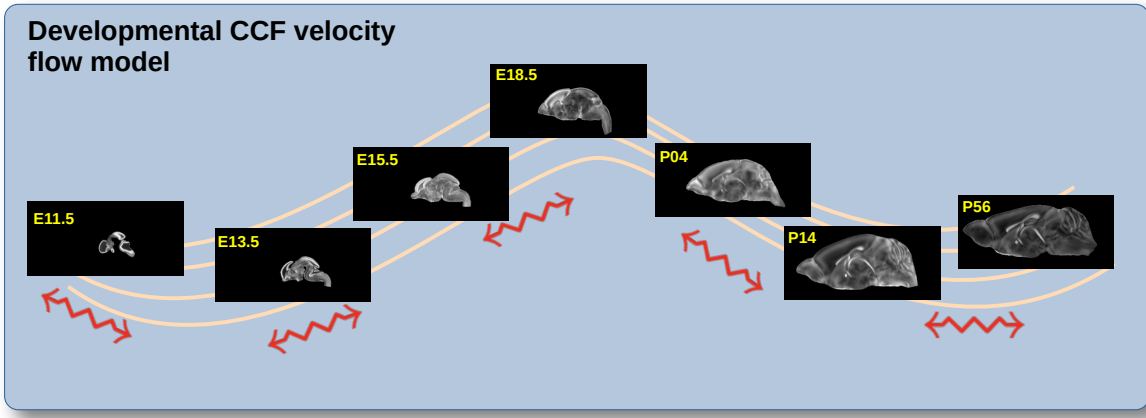


Figure 2: The spatial transformation between any two time points within the continuous DevCCF longitudinal developmental trajectory is available through the use of ANTsX functionality for generating a velocity flow model.

we developed a general velocity flow model approach which we apply to DevCCF-derived data. We also introduce this functionality into both the ANTsR and ANTsPy packages (for the latter, see `ants.fit_time_varying_transform_to_point_sets(...)`) for potential application to this and other analogous scenarios (e.g., modeling the cardiac and respiratory cycles). ANTsX, being built on top of ITK, uses an ITK image data structure for the 4-D velocity field where each voxel contains the x , y , z components of the field at that point.

2.2.1 Data

Labeled annotations are available as part of the original DevCCF and reside in the space of each developmental template which range in resolution from $31.5 - 50\mu\text{m}$. Across all atlases, the total number of labeled regions exceeds 2500. From these labels, a common set of 26 labels (13 per hemisphere) across all atlases were used for optimization and evaluation. These simplified regions include: terminal hypothalamus, subpallium, pallium, peduncular hypothalamus, prosomere, prosomere, prosomere, midbrain, prepontine hindbrain, pontine hindbrain, pontomedullary hindbrain, medullary hindbrain, and tracts (see Figure 3).

Prior to velocity field optimization, all data were rigidly transformed to DevCCF P56 using the centroids of the common label sets. In order to determine the landmark correspondence

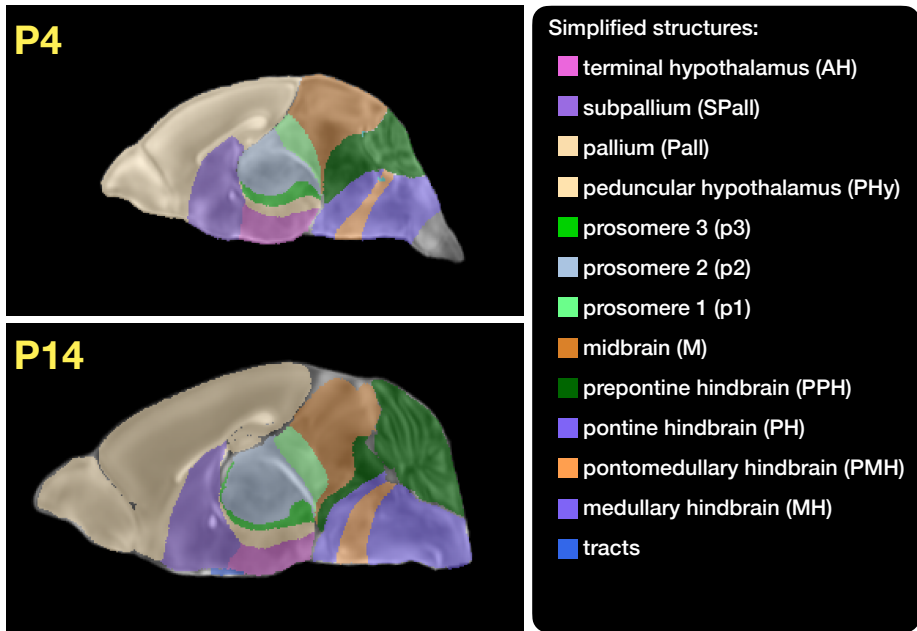


Figure 3: Annotated regions representing common labels across developmental stages which are illustrated for both P4 and P14.

239 across DevCCF stages, the multi-metric capabilities of `ants.registration(...)` were used.
 240 Instead of performing intensity-based pairwise registration directly on these multi-label im-
 241 ages, each label was used to construct a separate fixed and moving image pair resulting in a
 242 multi-metric registration optimization scenario involving 24 binary image pairs (each label
 243 weighted equally) for optimizing diffeomorphic correspondence between neighboring time
 244 point atlases using the mean squares metric and the symmetric normalization transform⁵⁰.
 245 To generate the set of common point sets across all seven developmental atlases, the label
 246 boundaries and whole regions were sampled in the P56 atlas and then propagated to each
 247 atlas using the transformations derived from the pairwise registrations. We selected a sam-
 248 pling rate of 10% for the contour points and 1% for the regional points for a total number
 249 of points being per atlas being 173303 ($N_{contour} = 98151$ and $N_{region} = 75152$). Regional
 250 boundary points were weighted twice as those of non-boundary points during optimization.

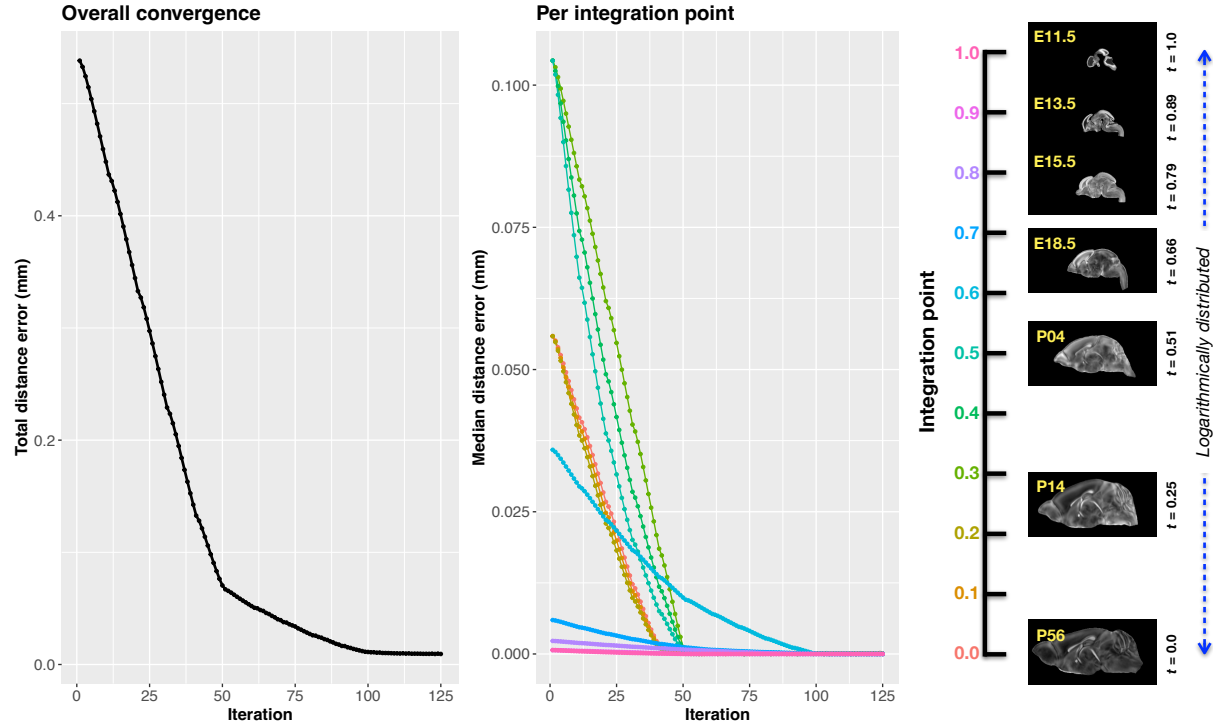


Figure 4: Convergence of the optimization of the velocity field for describing the transformation through the developmental stages from E11.5 through P56. Integration points in diagram on the right are color-coordinated with the center plot and placed in relation to the logarithmically situated temporal placement of the individual DevCCF atlases.

251 2.2.2 Velocity field optimization

252 The velocity field was optimized using the input composed of the seven corresponding point
 253 sets and their associated weight values, the selected number of integration points for the
 254 velocity field ($N = 11$), and the parameters defining the geometry of the spatial dimensions
 255 of the velocity field. Thus, the optimized velocity field described here is of size [256, 182, 360]
 256 ($50\mu\text{m}$ isotropic) $\times 11$ integration points for a total compressed size of a little over 2 GB.
 257 This choice represented weighing the trade-off between tractability, portability, and accuracy.
 258 However, all data and code to reproduce the results described are available in the dedicated
 259 GitHub repository.
 260 The normalized time point scalar value for each atlas/point-set in the temporal domains $[0, 1]$
 261 was also defined. Given the increasingly larger gaps in the postnatal time point sampling,
 262 we made two adjustments. Based on known mouse brain development, we used 28 days for

263 the P56 data. We then computed the log transform of the adjusted set of time points prior
264 to normalization between 0 and 1 (see the right side of Figure 4). This log transform, as
265 part of the temporal normalization, significantly improves the temporal spacing of data.

266 The maximum number of iterations was set to 200 with each iteration taking approximately
267 six minutes on a 2020 iMac (processor, 3.6 GHz 10-Core Intel Core i9; memory, 64 GB 2667
268 MHz DDR4) At each iteration we looped over the 11 integration points. At each integration
269 point, the velocity field estimate was updated by warping the two immediately adjacent
270 point sets to the integration time point and determining the regularized displacement field
271 between the two warped point sets. As with any gradient-based descent algorithm, this field
272 was multiplied by a small step size ($\delta = 0.2$) before adding to the current velocity field.
273 Convergence is determined by the average displacement error over each of the integration
274 points. As can be seen in the left panel of Figure 4, convergence occurred around 125
275 iterations when the average displacement error over all integration points is minimized. The
276 median displacement error at each of the integration points also trends towards zero but at
277 different rates.

278 2.2.3 The velocity flow transformation model

279 Once optimized, the resulting velocity field can be used to generate the deformable transform
280 between any two continuous points within the time interval bounded by E11.5 and P56. As
281 a demonstration, in Figure 5, we transform each atlas to the space of every other atlas
282 using the DevCCF transform model. Additionally, one can use this transformation model
283 to construct virtual templates in the temporal gaps of the DevCCF. Given an arbitrarily
284 chosen time point within the normalized time point interval, the existing adjacent DevCCF
285 atlases on either chronological side can be warped to the desired time point. A subsequent
286 call to one of the ANTsX template building functions then permits the construction of the
287 template at that time point. In Figure 6, we illustrate the use of the DevCCF velocity flow
288 model for generating two such virtual templates for two arbitrary time points. Note that
289 both of these usage examples can be found in the GitHub repository previously given.

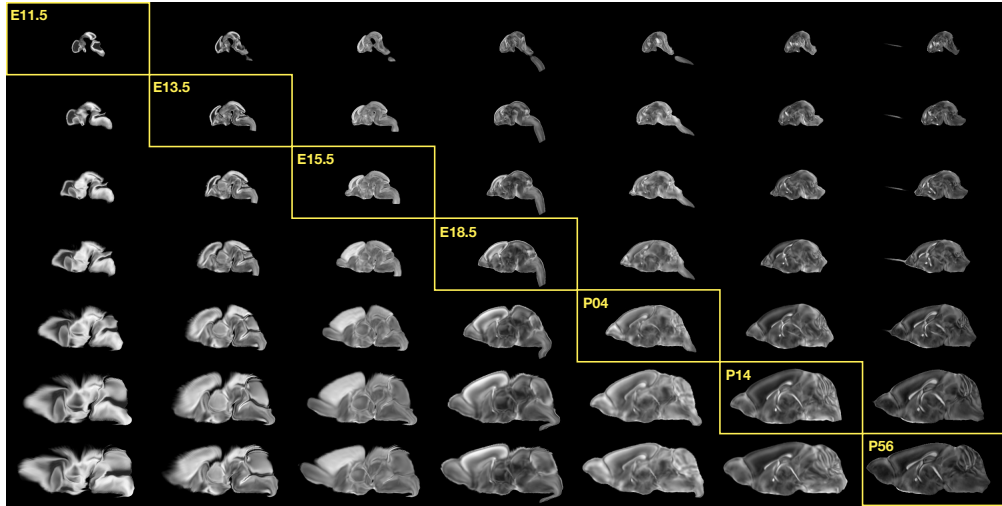


Figure 5: Mid-sagittal visualization of the effects of the transformation model in warping every developmental stage to the time point of every other developmental stage. The original images are located along the diagonal. Columns correspond to the warped original image whereas the rows represent the reference space to which each image is warped.

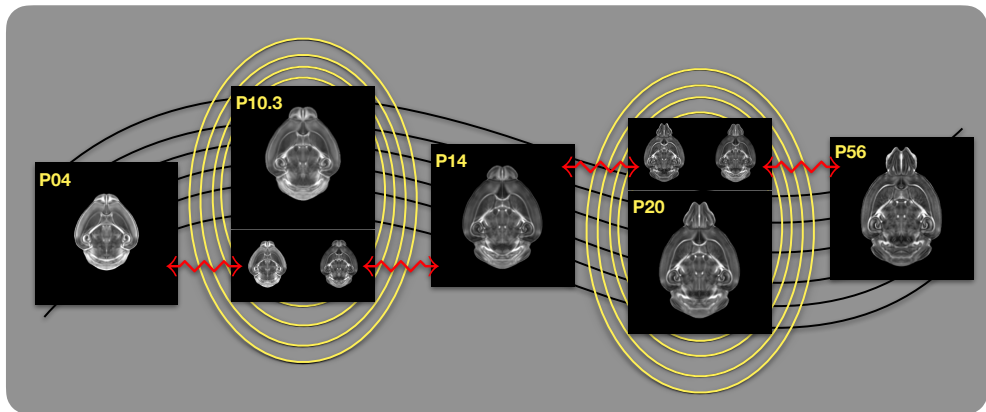


Figure 6: Illustration of the use of the velocity flow model for creating virtual templates at continuous time points not represented in one of the existing DevCCF time points. For example, FA templates at time point P10.3 and P20 can be generated by warping the existing temporally adjacent developmental templates to the target time point and using those images in the ANTsX template building process.

290 2.3 Automated structural parcellations of the mouse brain

291 Brain parcellation strategies for the mouse brain are pivotal for understanding the complex
292 organization and function of murine nervous system⁸¹. By dividing the brain into distinct
293 regions based on anatomical, physiological, or functional characteristics, researchers can
294 investigate specific areas in isolation and identify their roles in various behaviors and pro-

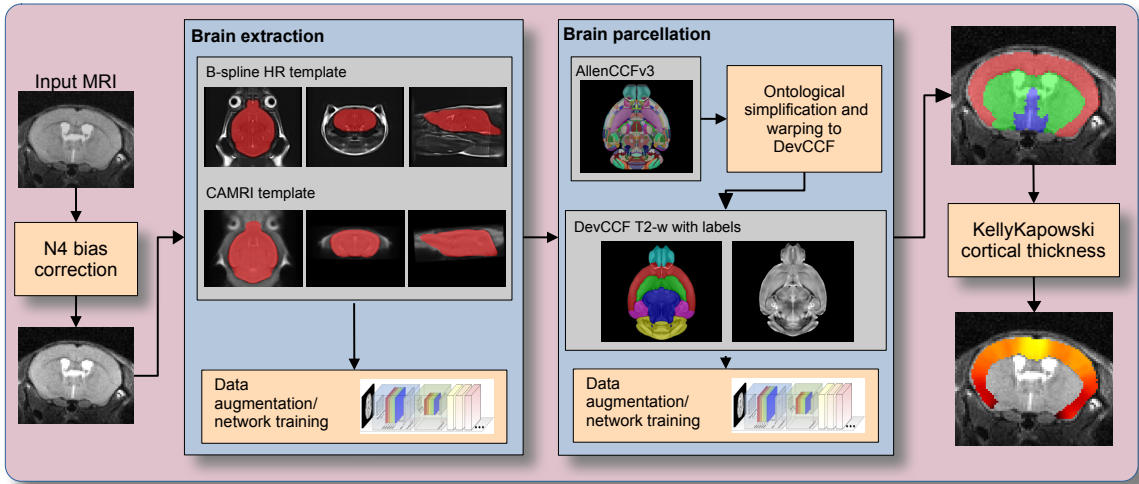


Figure 7: The mouse brain cortical parcellation pipeline integrating two deep learning components for brain extraction and brain parcellation prior to estimating cortical labels. Both deep learning networks rely heavily on aggressive data augmentation on templates built from open data and provide an outline for further refinement and creating alternative parcellations for tailored research objectives. Possible applications include voxelwise cortical thickness measurements.

cesses. For example, such parcellation schemes can help elucidate the spatial distribution of gene expression patterns⁸² as well as identify functional regions involved in specific cognitive tasks⁸³.

Although deep learning techniques have been used to develop useful parcellation tools for human brain research (e.g., SynthSeg⁸⁴, ANTsXNet⁴⁴), analogous development for the mouse brain is limited. In addition, mouse data is often characterized by unique imaging issues such as extreme anisotropic sampling which are often in sharp contrast to the high resolution template-based resources available within the community, e.g., AllenCCFv3 and DevCCF. We demonstrate how one can use the ANTsX tools to develop a complete mouse brain structural morphology pipeline as illustrated in Figure 7 and detailed below.

2.3.1 Few-shot mouse brain extraction network

In order to create a generalized mouse brain extraction network, we built whole-head templates from two publicly available datasets. The Center for Animal MRI (CAMRI) dataset⁶⁷ from the University of North Carolina at Chapel Hill consists of 16 T2-w MRI volumes of

309 voxel resolution $0.16 \times 0.16 \times 0.16 mm^3$. The second high-resolution dataset⁶⁸ comprises
310 88 specimens each with three spatially aligned canonical views with in-plane resolution of
311 $0.08 \times 0.08 mm^2$ with a slice thickness of $0.5 mm$. These three orthogonal views were used
312 to reconstruct a single high-resolution volume per subject using a B-spline fitting algorithm
313 available in ANTsX⁸⁵.

314 From these two datasets, two ANTsX templates⁵⁸ were generated. Bias field simulation,
315 intensity histogram warping, noise simulation, random translation and warping, and random
316 anisotropic resampling in the three canonical directions were used for data augmentation
317 in training an initial T2-w brain extraction network. This network was posted and the
318 corresponding functionality was immediately made available within ANTsXNet, similar to
319 our previous contributions to the community.

320 User interest led to a GitHub inquiry regarding possible study-specific improvements (<https://github.com/ANTsX/ANTsPyNet/issues/133>). This interaction led to the offering of a
321 user-made third template and extracted brain mask generated from T2-w ex-vivo data with
322 isotropic spacing of $0.08 mm$ in each voxel dimension. This third template, in conjunction
323 with the other two, were used with the same aggressive data augmentation to refine the
324 network weights which were subsequently posted and made available through ANTsPyNet
325 using the function `antspynet.mouse_brain_extraction(...)`.

327 2.3.2 Single-shot mouse brain parcellation network

328 AllenCCFv3 and its hierarchical ontological labeling, along with the DevCCF, provides the
329 necessary data for developing a tailored structural parcellation network for multi-modal
330 imaging. The `allensdk` Python library permits the creation of any gross parcellation based
331 on the AllenCCFv3 ontology. Specifically, using `allensdk` we coalesced the labels to the
332 following six major structures: cerebral cortex, cerebral nuclei, brain stem, cerebellum, main
333 olfactory bulb, and hippocampal formation. This labeling was mapped to the P56 component
334 of the DevCCF for use with the T2-w template component.

335 The T2-w P56 DevCCF and labelings, in conjunction with the data augmentation
336 described previously for brain extraction, were used to train the proposed brain

337 parcellation network. This is available in ANTsXNet (e.g. in ANTsPyNet using
 338 `antspynet.mouse_brain_parcellation(...)`). Note that other brain parcellation
 339 networks have also been trained using alternative regions and parcellation schemes and are
 340 available in the same ANTsXNet functionality. One usage note is that the data augmenta-
 341 tion used to train the network permits a learned interpolation in 0.08 mm isotropic space.
 342 Since the training data is isotropic and data augmentation includes downsampling in the
 343 canonical directions, each of the two networks learns mouse brain-specific interpolation such
 344 that one can perform prediction on thick-sliced images, as, for example, in these evaluation
 345 data, and return isotropic probability and thickness maps (a choice available to the user).
 346 This permits robust cortical thickness estimation even in the case of anisotropic data (see
 347 `antspynet.mouse_cortical_thickness(...)`).

348 **2.3.3 Evaluation**

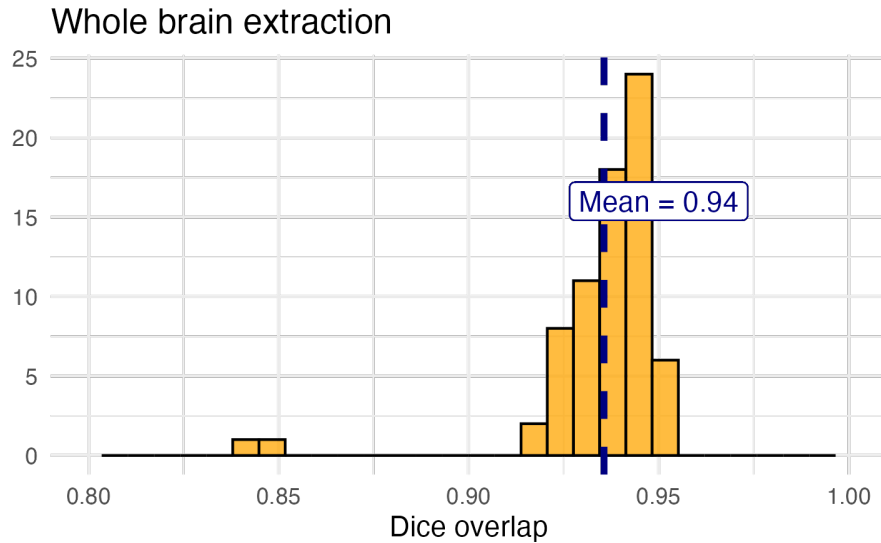
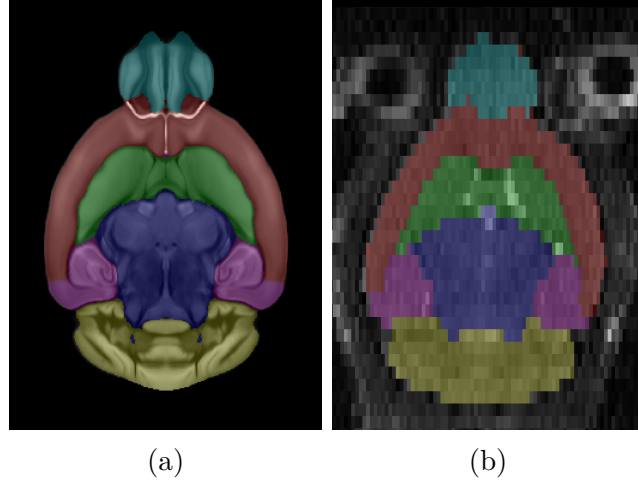


Figure 8: Evaluation of the ANTsX mouse brain extraction on an independent, publicly available dataset consisting of 12 specimens \times 7 time points = 84 total images. Dice overlap comparisons with the user-generated brain masks provide good agreement with the automated results from the brain extraction network.

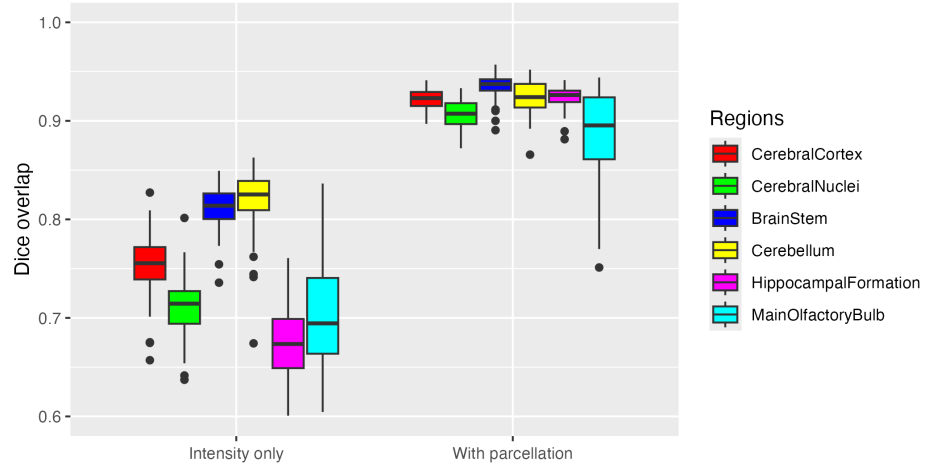
349 For evaluation, we used an additional publicly available dataset⁶⁹ that is completely inde-
 350 pendent from the data used in training the brain extraction and parcellation networks. Data
 351 includes 12 specimens each imaged at seven time points (Day 0, Day 3, Week 1, Week 4,



(a)

(b)

Normalization to AllenCCFv3



(c)

Figure 9: Evaluation of the ANTsX mouse brain parcellation on the same dataset. (a) T2-w DevCCF P56 with the described parcellation consisting of the cerebral cortex, nuclei, brain stem, cerebellum, main olfactory bulb, and hippocampal formation. (b) Sample subject (NR5 Day 0) with the proposed deep learning-based segmentation. (c) Dice overlap for comparing the regional alignments between registration using intensity information only and using intensity with the given parcellation scheme.

352 Week 8, Week 20) with in-house-generated brain masks for a total of 84 images. Spacing is
353 anisotropic with an in-plane resolution of $0.1 \times 0.1 mm^2$ and a slice thickness of $0.5 mm$.

354 Figure 8 summarizes the whole brain overlap between the provided segmentations for all
355 84 images and the results of applying the proposed network. Also, since mapping to the
356 AllenCCFv3 atlas is crucial for many mouse studies, we demonstrate the utility of the second
357 network by leveraging the labeled regions to perform anatomically-explicit alignment using
358 ANTsX multi-component registration instead of intensity-only registration. For these data,
359 the whole brain extraction demonstrates excellent performance across the large age range.
360 And although the intensity-only image registration provides adequate alignment, intensity
361 with the regional parcellations significantly improves those measures.

362 **3 Discussion**

363 The diverse mouse brain cell type profiles gathered through BICCN and associated efforts
364 provide a rich multi-modal resource to the research community. However, despite significant
365 progress, optimal leveraging of these valuable resources remains an ongoing challenge. A
366 central component to data integration is accurately mapping novel cell type data into com-
367 mon coordinate frameworks (CCFs) for subsequent processing and analysis. To meet these
368 needs, tools for mapping mouse brain data must be both broadly accessible and capable of
369 addressing challenges unique to each modality. In this work, we described modular ANTsX-
370 based pipelines developed to support three distinct BICCN efforts encompassing spatial
371 transcriptomic, morphological, and developmental data. We demonstrated how a flexible
372 image analysis toolkit like ANTsX can be tailored to address specific modality-driven con-
373 straints by leveraging reusable, validated components.

374 The MERFISH mapping pipeline illustrates how ANTsX tools can be adapted to accom-
375 modate high-resolution spatial transcriptomic data. While the general mapping strategy is
376 applicable to other sectioned histological data, the pipeline includes specific adjustments for
377 known anatomical and imaging artifacts present in MERFISH datasets. As such, this exam-
378 ple demonstrates how general-purpose tools can be customized to meet the requirements of
379 highly specialized data types.

380 The fMOST mapping pipeline was developed with the intention of broader applicability.
381 Built primarily from existing ANTsX preprocessing and registration modules, this pipeline
382 introduces an fMOST-specific intermediate atlas to facilitate consistent mappings to the
383 AllenCCFv3. The use of a canonical fMOST atlas reduces the need for repeated manual
384 alignment across new datasets, and the resulting transformations can be directly applied to
385 associated single-neuron reconstructions. This supports integrative morphological analysis
386 across specimens using a common coordinate system.

387 For developmental data, we introduced a velocity field-based model for continuous interpo-
388 lation between discrete DevCCF timepoints. Although the DevCCF substantially expands
389 coverage of developmental stages relative to prior atlases, temporal gaps remain. The ve-

390 locity model enables spatio-temporal transformations within the full developmental interval
391 and supports the generation of virtual templates at unsampled ages. This functionality is
392 built using ANTsX components for velocity field optimization and integration, and offers
393 a novel mechanism for interpolating across the non-linear developmental trajectory of the
394 mouse brain. Such interpolation has potential utility for both anatomical harmonization and
395 longitudinal analyses.

396 We also introduced a template-based deep learning pipeline for mouse brain extraction and
397 parcellation using aggressive data augmentation. This approach is designed to reduce the
398 reliance on large annotated training datasets, which remain limited in the mouse imaging
399 domain. Evaluation on independent data demonstrates promising generalization, though
400 further refinement will be necessary. As with our human-based ANTsX pipelines, failure
401 cases can be manually corrected and recycled into future training cycles. Community con-
402 tributions are welcomed and encouraged, providing a pathway for continuous improvement
403 and adaptation to new datasets.

404 The ANTsX ecosystem offers a powerful foundation for constructing scalable, reproducible
405 pipelines for mouse brain data analysis. Its modular design and multi-platform support
406 enable researchers to develop customized workflows without extensive new software devel-
407 opment. The widespread use of ANTsX components across the neuroimaging community
408 attests to its utility and reliability. As a continuation of the BICCN program, ANTsX is
409 well positioned to support the goals of the BRAIN Initiative Cell Atlas Network (BICAN)
410 and future efforts to extend these mapping strategies to the human brain.

411 4 Methods

412 The following methods are all available as part of the ANTsX ecosystem with analogous
413 elements existing in both ANTsR (ANTs in R) and ANTsPy (ANTs in Python), under-
414 pinned by a shared ANTs/ITK C++ core. Most development for the work described was
415 performed using ANTsPy. For equivalent functionality in ANTsR, we refer the reader to the
416 comprehensive ANTsX tutorial: <https://tinyurl.com/antsxtutorial>.

417 4.1 General ANTsX utilities

418 Although focused on distinct data types, the three pipelines presented in this work share
419 common components that address general challenges in mapping mouse brain data. These
420 include correcting image intensity artifacts, denoising, spatial registration, template gen-
421 eration, and visualization. Table 1 provides a concise summary of the relevant ANTsX
422 functionality.

423 **Preprocessing: bias field correction and denoising.** Standard preprocessing steps in
424 mouse brain imaging include correcting for spatial intensity inhomogeneities and reducing im-
425 age noise, both of which can impact registration accuracy and downstream analysis. ANTsX
426 provides implementations of widely used methods for these tasks. The N4 bias field correction
427 algorithm⁵¹, originally developed in ANTs and contributed to ITK, mitigates artifactual, low-
428 frequency intensity variation and is accessible via `ants.n4_bias_field_correction(...)`.
429 Patch-based denoising⁶⁰ has been implemented as `ants.denoise_image(...)`.

430 **Image registration.** ANTsX includes a robust and flexible framework for pairwise
431 and groupwise image registration⁸⁶. At its core is the SyN algorithm⁵⁰, a symmetric
432 diffeomorphic model with optional B-spline regularization⁶⁶. In ANTsPy, registration
433 is performed via `ants.registration(...)` using preconfigured parameter sets (e.g.,
434 `antsRegistrationSyNQuick[s]`, `antsRegistrationSyN[s]`) suitable for different imaging
435 modalities and levels of computational demand. Resulting transformations can be applied
436 to new images with `ants.apply_transforms(...)`.

Table 1: Sampling of ANTsX functionality

<i>ANTsPy: Preprocessing</i>	
bias field correction	<code>n4_bias_field_correction(...)</code>
image denoising	<code>denoise_image(...)</code>
<i>ANTsPy: Registration</i>	
image registration	<code>registration(...)</code>
image transformation	<code>apply_transforms(...)</code>
template generation	<code>build_template(...)</code>
landmark registration	<code>fit_transform_to_paired_points(...)</code>
time-varying landmark reg.	<code>fit_time_varying_transform_to_point_sets(...)</code>
integrate velocity field	<code>integrate_velocity_field(...)</code>
invert displacement field	<code>invert_displacement_field(...)</code>
<i>ANTsPy: Segmentation</i>	
MRF-based segmentation	<code>atropos(...)</code>
Joint label fusion	<code>joint_label_fusion(...)</code>
diffeomorphic thickness	<code>kelly_kapowski(...)</code>
<i>ANTsPy: Miscellaneous</i>	
Regional intensity statistics	<code>label_stats(...)</code>
Regional shape measures	<code>label_geometry_measures(...)</code>
B-spline approximation	<code>fit_bspline_object_to_scattered_data(...)</code>
Visualize images and overlays	<code>plot(...)</code>
<i>ANTsPyNet: Mouse-specific</i>	
brain extraction	<code>mouse_brain_extraction(...modality="t2"...)</code>
brain parcellation	<code>mouse_brain_parcellation(...)</code>
cortical thickness	<code>mouse_cortical_thickness(...)</code>
super resolution	<code>mouse_histology_super_resolution(...)</code>

ANTsX provides state-of-the-art functionality for processing biomedical image data. Such tools, including deep learning networks, support a variety of mapping-related tasks. A more comprehensive listing of ANTsX tools with self-contained R and Python examples is provided as a gist page on GitHub (<https://tinyurl.com/antsxtutorial>).

437 **Template generation.** ANTsX supports population-based template generation through it-
438 erative pairwise registration to an evolving estimate of the mean shape and intensity reference
439 space across subjects⁵⁸. This functionality was used in generating the DevCCF templates¹⁶.
440 The procedure, implemented as `ants.build_template(...)`, produces average images in
441 both shape and intensity by aligning all inputs to a common evolving template.

442 **Visualization.** To support visual inspection and quality control, ANTsPy provides flexible
443 image visualization with `ants.plot(...)`. This function enables multi-slice and multi-
444 orientation rendering with optional overlays and label maps.

445 4.2 Mapping fMOST data to AllenCCFv3

446 **Preprocessing.** Mapping fMOST data into the AllenCCFv3 presents unique challenges due
447 to its native ultra-high resolution and imaging artifacts common to the fMOST modality.
448 Each fMOST image can exceed a terabyte in size, with spatial resolutions far exceeding
449 those of the AllenCCFv3 ($25\text{ }\mu\text{m}$ isotropic). To reduce computational burden and prevent
450 resolution mismatch, each fMOST image is downsampled using cubic B-spline interpolation
451 via `ants.resample_image(...)` to match the template resolution.

452 Stripe artifacts (i.e., periodic intensity distortions caused by nonuniform sectioning or il-
453 lumination) are common in fMOST and can mislead deformable registration algorithms.
454 These were removed using a custom 3D notch filter (`remove_stripe_artifact(...)`) im-
455 plemented in the `CCFAlignmentToolkit` using SciPy frequency domain filtering. The filter
456 targets dominant stripe frequencies along a user-specified axis in the Fourier domain. In
457 addition, intensity inhomogeneity across sections, often arising from variable staining or
458 illumination, was corrected using N4 bias field correction.

459 **Template-based spatial normalization.** To facilitate reproducible mapping, we first
460 constructed a contralaterally symmetric average template from 30 fMOST brains and their
461 mirrored counterparts using ANTsX template-building tools. Because the AllenCCFv3 and
462 fMOST data differ substantially in both intensity contrast and morphology, direct deformable
463 registration between individual fMOST brains and the AllenCCFv3 was insufficiently robust.

464 Instead, we performed a one-time expert-guided label-driven registration between the aver-
465 age fMOST template and AllenCCFv3. This involved sequential alignment of seven manually
466 selected anatomical regions: 1) brain mask/ventricles, 2) caudate/putamen, 3) fimbria, 4)
467 posterior choroid plexus, 5) optic chiasm, 6) anterior choroid plexus, and 7) habenular
468 commissure which were prioritized to enable coarse-to-fine correction of shape differences.
469 Once established, this fMOST-template-to-AllenCCFv3 transform was reused for all subse-
470 quent specimens. Each new fMOST brain was then registered to the average fMOST tem-
471 plate using intensity-based registration, followed by concatenation of transforms to produce
472 the final mapping into AllenCCFv3 space.

473 **Mapping neuron projections.** A key advantage of fMOST imaging is its ability to support
474 single neuron projection reconstruction across the entire brain⁷⁹. Because these reconstruc-
475 tions are stored as 3D point sets aligned to the original fMOST volume, we applied the same
476 composite transform used for image alignment to the point data using ANTsX functional-
477 ity. This enables seamless integration of cellular morphology data into AllenCCFv3 space,
478 facilitating comparative analyses across specimens.

479 4.3 Mapping MERFISH data to AllenCCFv3

480 **Preprocessing.** MERFISH data are acquired as a series of 2D tissue sections, each com-
481 prising spatially localized gene expression measurements at subcellular resolution. To enable
482 3D mapping to the AllenCCFv3, we first constructed anatomical reference images by aggre-
483 gating the number of detected transcripts per voxel across all probes within each section.
484 These 2D projections were resampled to a resolution of $10 \mu m \times 10 \mu m$ to match the in-plane
485 resolution of the AllenCCFv3.

486 Sections were coarsely aligned using manually annotated dorsal and ventral midline points,
487 allowing initial volumetric reconstruction. However, anatomical fidelity remained limited by
488 variation in section orientation, spacing, and tissue loss. To further constrain alignment and
489 enable deformable registration, we derived region-level anatomical labels directly from the
490 gene expression data.

491 **Label creation.** We assigned each detected cell to one of 15 coarse anatomical regions (e.g.,
492 hippocampus, cortex, striatum—using transcriptomic similarity to scRNA) seq reference
493 data. These assignments were aggregated across spatial grids to produce probabilistic label
494 maps for each section. To ensure full regional coverage, morphological dilation was applied to
495 fill gaps between sparsely distributed cells. Finer-resolution structures (e.g., cortical layers,
496 habenula) were similarly labeled using marker gene enrichment and spatial constraints. This
497 dual-level labeling (i.e., coarse and fine) allowed us to construct a robust anatomical scaffold
498 in the MERFISH coordinate system that could be matched to AllenCCFv3 annotations.

499 **Section matching via global alignment.** A major challenge was compensating for oblique
500 cutting angles and non-uniform section thickness, which distort the anatomical shape and
501 spacing of the reconstructed volume. Rather than directly warping the MERFISH data
502 into atlas space, we globally aligned the AllenCCFv3 to the MERFISH coordinate system.
503 This was done via an affine transformation followed by resampling of AllenCCFv3 sections
504 to match the number and orientation of MERFISH sections. This approach minimizes
505 interpolation artifacts in the MERFISH data and facilitates one-to-one section matching.

506 **Landmark-driven deformable alignment.** We used a 2.5D approach for fine alignment of
507 individual sections. In each MERFISH slice, deformable registration was driven by sequential
508 alignment of anatomical landmarks between the label maps derived from MERFISH and
509 AllenCCFv3. A total of nine regions—including isocortical layers 2/3, 5, and 6, the striatum,
510 hippocampus, thalamus, and medial/lateral habenula—were registered in an empirically
511 determined order. After each round, anatomical alignment was visually assessed by an
512 expert, and the next structure was selected to maximize improvement in the remaining
513 misaligned regions.

514 The final transform for each section combined the global affine alignment and the per-
515 structure deformable registrations. These were concatenated to generate a 3D mapping from
516 the original MERFISH space to the AllenCCFv3 coordinate system. Once established, the
517 composite mapping enables direct transfer of gene-level and cell-type data from MERFISH
518 into atlas space, allowing integration with other imaging and annotation datasets.

519 **4.4 DevCCF velocity flow transformation model**

520 The Developmental Common Coordinate Framework (DevCCF)¹⁶ provides a discrete set of
521 age-specific templates that temporally sample the developmental trajectory. To model this
522 biological progression more continuously, we introduce a velocity flow-based paradigm for in-
523 ferring diffeomorphic transformations between developmental stages. This enables anatomi-
524 cally plausible estimation of intermediate templates or mappings at arbitrary timepoints
525 between the E11.5 and P56 endpoints of the DevCCF. Our approach builds on established
526 insights from time-varying diffeomorphic registration⁶⁵, where a velocity field governs the
527 smooth deformation of anatomical structures over time. Importantly, the framework is ex-
528 tensible and can naturally accommodate additional timepoints for the potential expansion
529 of the DevCCF.

530 **Point sampling and region correspondence.** We first coalesced the anatomical labels
531 across the seven DevCCF templates (E11.5, E13.5, E15.5, E18.5, P4, P14, P56) into 26
532 common structures that could be consistently identified across development. These include
533 major brain regions such as the cortex, cerebellum, hippocampus, midbrain, and ventricles.
534 For each successive pair of templates, we performed multi-label deformable registration us-
535 ing ANTsX to generate forward and inverse transforms between anatomical label volumes.
536 From the P56 space, we randomly sampled approximately $1e6$ points within and along the
537 boundaries of each labeled region and propagated them through each pairwise mapping step
538 (e.g., P56 \rightarrow P14, P14 \rightarrow P4, ..., E13.5 \rightarrow E11.5). This procedure created time-indexed
539 point sets tracing the spatial evolution of each region.

540 **Velocity field fitting.** Using these point sets, we fit a continuous velocity field over devel-
541 opmental time using a generalized B-spline scattered data approximation method [85], which
542 is implemented in ANTsX and ITK. The field was parameterized over a log-scaled time
543 axis to ensure finer temporal resolution during early embryonic stages, where morphological
544 changes are most rapid. Optimization proceeded for approximately 125 iterations, minimiz-
545 ing the average Euclidean norm between transformed points at each step. Ten integration
546 points were used to ensure numerical stability. The result is a smooth, differentiable vector
547 field that defines a diffeomorphic transform between any two timepoints within the template

548 range.

549 **Applications and availability.** This velocity model can be used to estimate spatial trans-
550 formations between any pair of developmental stages—even those for which no empirical
551 template exists—allowing researchers to create interpolated atlases, align new datasets, or
552 measure continuous structural changes. It also enables developmental alignment of multi-
553 modal data (e.g., MRI to LSFM) by acting as a unifying spatiotemporal scaffold. The imple-
554 mentation is accessible via `ants.fit_time_varying_transform_to_point_sets(...)` in
555 ANTsPy, and we include reproducible examples in our public codebase.

556 4.5 ANTsXNet mouse brain applications

557 To support template-based deep learning approaches for structural brain extraction and par-
558 cellation, we implemented dedicated pipelines using the ANTsXNet framework. ANTsXNet
559 comprises open-source deep learning libraries in both Python (ANTsPyNet) and R (ANTsR-
560 Net) that interface with the broader ANTsX ecosystem and are built on TensorFlow/Keras.
561 Our mouse brain pipelines mirror existing ANTsXNet tools for human imaging but are
562 adapted for species-specific anatomical variation, lower SNR, and heterogeneous acquisition
563 protocols.

564 4.5.1 Deep learning training setup

565 All networks were implemented in ANTsPyNet using standard 3D U-net architectures [87].
566 Training was performed on an NVIDIA DGX system (4× Tesla V100 GPUs, 256 GB RAM).
567 Model weights and preprocessing routines are shared across ANTsPyNet and ANTsRNet to
568 ensure reproducibility and language portability. Public training scripts and data generators
569 are available at <https://github.com/ntustison/ANTsXNetTraining>.

570 **Data augmentation.** Robust data augmentation was critical to generalization across scan-
571 ners, contrast types, and resolutions. We applied both intensity- and shape-based augmen-
572 tation strategies:

- 573 • *Intensity augmentations:*

- 574 – Gaussian, Poisson, and salt-and-pepper noise: `ants.add_noise_to_image(...)`
575 – Simulated intensity inhomogeneity via bias field modeling: `antspynet.simulate_bias_field(...)`
576 – Histogram warping to simulate contrast variation: `antspynet.histogram_warp_image_intensi`
- 577 • *Shape augmentations:*
- 578 – Random nonlinear deformations and affine transforms: `antspynet.randomly_transform_image(...)`
579 – Anisotropic resampling across axial, sagittal, and coronal planes: `ants.resample_image(...)`

580 4.5.2 Brain extraction

581 We trained a mouse-specific brain extraction model on two manually masked T2-
582 weighted templates, generated from public datasets [^{68,67}]. One of the templates was
583 constructed from orthogonal 2D acquisitions using B-spline-based volumetric synthesis via
584 `ants.fit_bspline_object_to_scattered_data(...)`. Normalized gradient magnitude
585 was used as a weighting function to emphasize boundaries during reconstruction.

586 This training strategy provides strong spatial priors despite limited data — leveraging high-
587 quality template data and aggressive augmentation to mimic population variability. The
588 final trained network is available via ANTsXNet:

- 589 • Template: `antspynet.get_antsxnet_data("bsplineT2MouseTemplate")`
590 • Brain mask: `antspynet.get_antsxnet_data("bsplineT2MouseTemplateBrainMask")`

591 4.5.3 Brain parcellation

592 For brain parcellation, we trained a 3D U-net model using the DevCCF P56 T2-weighted
593 template and anatomical segmentations derived from AllenCCFv3. This template-based
594 training strategy allows the model to produce accurate, multi-region parcellations without
595 requiring large-scale annotated subject data.

596 To harmonize intensity across specimens, input images were preprocessed using rank-based
597 intensity normalization (`ants.rank_intensity(...)`). Spatial harmonization was achieved

598 by affine and deformable alignment of each extracted brain to the P56 template prior to
599 inference. In addition to the normalized image input, the network also receives prior proba-
600 bility maps derived from the atlas segmentations, providing additional spatial context. These
601 resources are available via `get_antsxnet_data(...)`.

602 **4.5.4 Evaluation and reuse**

603 To assess model generalizability, both brain extraction and parcellation models were eval-
604 uated on an external longitudinal dataset [69] with varied scanning parameters. The pipeline
605 demonstrated robust performance without retraining, highlighting the utility of a template-
606 driven, low-shot approach. All models, training scripts, and data resources are publicly
607 available and designed for plug-and-play use within ANTsX workflows.

608 **Data availability**

609 All data and software used in this work are publicly available. The DevCCF atlas is
610 available at <https://kimlab.io/brain-map/DevCCF/>. ANTsPy, ANTsR, ANTsPyNet, and
611 ANTsRNet are available through GitHub at the ANTsX Ecosystem ([https://github.com/](https://github.com/ANTsX)
612 [ANTsX](#)). Training scripts for all deep learning functionality in ANTsXNet can also be
613 found on GitHub (<https://github.com/ntustison/ANTsXNetTraining>). A GitHub reposi-
614 tory specifically pertaining to the AllenCCFv3 mapping is available at <https://github.com/>
615 [dontminchenit/CCFAAlignmentToolkit](#). For the other two contributions contained in this
616 work, the longitudinal DevCCF mapping and mouse cortical thickness pipeline, we refer the
617 interested reader to <https://github.com/ntustison/ANTsXMouseBrainMapping>.

618 **Acknowledgments**

619 Support for the research reported in this work includes funding from the National Institute
620 of Biomedical Imaging and Bioengineering (R01-EB031722) and National Institute of Mental
621 Health (RF1-MH124605 and U24-MH114827).

622 We also acknowledge the data contribution of Dr. Adam Raikes (GitHub @araikes) of the
623 Center for Innovation in Brain Science at the University of Arizona for refining the weights
624 of the mouse brain extraction network.

625 **Author contributions**

626 N.T., M.C., and J.G. wrote the main manuscript text and figures. M.C., M.K., R.D., S.S.,
627 Q.W., L.G., J.D., C.G., and J.G. developed the Allen registration pipelines. N.T. and F.K.
628 developed the time-varying velocity transformation model for the DevCCF. N.T. and M.T.
629 developed the brain parcellation and cortical thickness methodology. All authors reviewed
630 the manuscript.

631 **References**

- 632 1. Keller, P. J. & Ahrens, M. B. Visualizing whole-brain activity and development at
the single-cell level using light-sheet microscopy. *Neuron* **85**, 462–83 (2015).
- 633 2. La Manno, G. *et al.* Molecular architecture of the developing mouse brain. *Nature*
596, 92–96 (2021).
- 634 3. Wen, L. *et al.* Single-cell technologies: From research to application. *Innovation
(Camb)* **3**, 100342 (2022).
- 635 4. Oh, S. W. *et al.* A mesoscale connectome of the mouse brain. *Nature* **508**, 207–14
(2014).
- 636 5. Gong, H. *et al.* Continuously tracing brain-wide long-distance axonal projections in
mice at a one-micron voxel resolution. *Neuroimage* **74**, 87–98 (2013).
- 637 6. Li, A. *et al.* Micro-optical sectioning tomography to obtain a high-resolution atlas of
the mouse brain. *Science* **330**, 1404–8 (2010).
- 638 7. Ueda, H. R. *et al.* Tissue clearing and its applications in neuroscience. *Nat Rev
Neurosci* **21**, 61–79 (2020).
- 639 8. Ståhl, P. L. *et al.* Visualization and analysis of gene expression in tissue sections by
spatial transcriptomics. *Science* **353**, 78–82 (2016).
- 640 9. Burgess, D. J. Spatial transcriptomics coming of age. *Nat Rev Genet* **20**, 317 (2019).
- 641 10. Hardwick, S. A. *et al.* Single-nuclei isoform RNA sequencing unlocks barcoded exon
connectivity in frozen brain tissue. *Nature biotechnology* **40**, 1082–1092 (2022).
- 642 11. Hawrylycz, M. *et al.* A guide to the BRAIN initiative cell census network data
ecosystem. *PLoS biology* **21**, e3002133 (2023).
- 643 12. Wang, Q. *et al.* The allen mouse brain common coordinate framework: A 3D reference
atlas. *Cell* **181**, 936–953.e20 (2020).
- 644 13. Perens, J. *et al.* An optimized mouse brain atlas for automated mapping and quantification
of neuronal activity using iDISCO+ and light sheet fluorescence microscopy.
Neuroinformatics **19**, 433–446 (2021).
- 645 14. Ma, Y. *et al.* A three-dimensional digital atlas database of the adult C57BL/6J mouse
brain by magnetic resonance microscopy. *Neuroscience* **135**, 1203–1215 (2005).

- 646 15. Qu, L. *et al.* Cross-modal coherent registration of whole mouse brains. *Nature Methods* **19**, 111–118 (2022).
- 647 16. Kronman, F. N. *et al.* Developmental mouse brain common coordinate framework. *Nat Commun* **15**, 9072 (2024).
- 648 17. Chuang, N. *et al.* An MRI-based atlas and database of the developing mouse brain. *Neuroimage* **54**, 80–89 (2011).
- 649 18. Dries, R. *et al.* Advances in spatial transcriptomic data analysis. *Genome research* **31**, 1706–1718 (2021).
- 650 19. Ricci, P. *et al.* Removing striping artifacts in light-sheet fluorescence microscopy: A review. *Progress in biophysics and molecular biology* **168**, 52–65 (2022).
- 651 20. Agarwal, N., Xu, X. & Gopi, M. Robust registration of mouse brain slices with severe histological artifacts. in *Proceedings of the tenth indian conference on computer vision, graphics and image processing* 1–8 (2016).
- 652 21. Agarwal, N., Xu, X. & Gopi, M. Automatic detection of histological artifacts in mouse brain slice images. in *Medical computer vision and bayesian and graphical models for biomedical imaging: MICCAI 2016 international workshops, MCV and BAMBI, athens, greece, october 21, 2016, revised selected papers* 8 105–115 (Springer, 2017).
- 653 22. Tward, D. *et al.* 3d mapping of serial histology sections with anomalies using a novel robust deformable registration algorithm. in *International workshop on multimodal brain image analysis* 162–173 (Springer, 2019).
- 654 23. Cahill, L. S. *et al.* Preparation of fixed mouse brains for MRI. *Neuroimage* **60**, 933–939 (2012).
- 655 24. Sunkin, S. M. *et al.* Allen brain atlas: An integrated spatio-temporal portal for exploring the central nervous system. *Nucleic acids research* **41**, D996–D1008 (2012).
- 656 25. Kim, Y. *et al.* Brain-wide maps reveal stereotyped cell-type-based cortical architecture and subcortical sexual dimorphism. *Cell* **171**, 456–469 (2017).
- 657 26. Fürth, D. *et al.* An interactive framework for whole-brain maps at cellular resolution. *Nat Neurosci* **21**, 139–149 (2018).

- 658 27. Li, Y. *et al.* mBrainAligner-web: A web server for cross-modal coherent registration
of whole mouse brains. *Bioinformatics* **38**, 4654–4655 (2022).
- 659 28. Puchades, M. A., Csucs, G., Ledergerber, D., Leergaard, T. B. & Bjaalie, J. G. Spatial
registration of serial microscopic brain images to three-dimensional reference atlases
with the QuickNII tool. *PloS one* **14**, e0216796 (2019).
- 660 29. Eastwood, B. S. *et al.* Whole mouse brain reconstruction and registration to a ref-
erence atlas with standard histochemical processing of coronal sections. *Journal of
Comparative Neurology* **527**, 2170–2178 (2019).
- 661 30. Ni, H. *et al.* A robust image registration interface for large volume brain atlas. *Sci
Rep* **10**, 2139 (2020).
- 662 31. Pallast, N. *et al.* Processing pipeline for atlas-based imaging data analysis of struc-
tural and functional mouse brain MRI (AIDAmri). *Front Neuroinform* **13**, 42 (2019).
- 663 32. Celestine, M., Nadkarni, N. A., Garin, C. M., Bougacha, S. & Dhenain, M. **Sammbar-
MRI: A library for processing SmAll-MaMmal BrAin MRI data in python.** *Front
Neuroinform* **14**, 24 (2020).
- 664 33. Ioanas, H.-I., Marks, M., Zerbi, V., Yanik, M. F. & Rudin, M. **An optimized regis-
tration workflow and standard geometric space for small animal brain imaging.** *Neu-
roimage* **241**, 118386 (2021).
- 665 34. Aggarwal, M., Zhang, J., Miller, M. I., Sidman, R. L. & Mori, S. Magnetic resonance
imaging and micro-computed tomography combined atlas of developing and adult
mouse brains for stereotaxic surgery. *Neuroscience* **162**, 1339–1350 (2009).
- 666 35. Chandrashekhar, V. *et al.* CloudReg: Automatic terabyte-scale cross-modal brain
volume registration. *Nature methods* **18**, 845–846 (2021).
- 667 36. Jin, M. *et al.* **SMART: An open-source extension of WholeBrain for intact mouse
brain registration and segmentation.** *eNeuro* **9**, (2022).
- 668 37. Negwer, M. *et al.* **FriendlyClearMap: An optimized toolkit for mouse brain mapping
and analysis.** *Gigascience* **12**, (2022).
- 669 38. Lin, W. *et al.* Whole-brain mapping of histaminergic projections in mouse brain.
Proceedings of the National Academy of Sciences **120**, e2216231120 (2023).

- 670 39. Zhang, M. *et al.* Spatially resolved cell atlas of the mouse primary motor cortex by MERFISH. *Nature* **598**, 137–143 (2021).
- 671 40. Shi, H. *et al.* Spatial atlas of the mouse central nervous system at molecular resolution. *Nature* **622**, 552–561 (2023).
- 672 41. Zhang, Y. *et al.* Reference-based cell type matching of *in situ* image-based spatial transcriptomics data on primary visual cortex of mouse brain. *Scientific Reports* **13**, 9567 (2023).
- 673 42. Klein, S., Staring, M., Murphy, K., Viergever, M. A. & Pluim, J. P. W. [Elastix: A toolbox for intensity-based medical image registration](#). *IEEE Trans Med Imaging* **29**, 196–205 (2010).
- 674 43. Fedorov, A. *et al.* 3D slicer as an image computing platform for the quantitative imaging network. *Magnetic resonance imaging* **30**, 1323–1341 (2012).
- 675 44. Tustison, N. J. *et al.* [The ANTsX ecosystem for quantitative biological and medical imaging](#). *Sci Rep* **11**, 9068 (2021).
- 676 45. Rolfe, S. M., Whikehart, S. M. & Maga, A. M. [Deep learning enabled multi-organ segmentation of mouse embryos](#). *Biol Open* **12**, bio059698 (2023).
- 677 46. Pagani, M., Damiano, M., Galbusera, A., Tsafaris, S. A. & Gozzi, A. Semi-automated registration-based anatomical labelling, voxel based morphometry and cortical thickness mapping of the mouse brain. *Journal of neuroscience methods* **267**, 62–73 (2016).
- 678 47. Anderson, R. J. *et al.* [Small animal multivariate brain analysis \(SAMBA\) - a high throughput pipeline with a validation framework](#). *Neuroinformatics* **17**, 451–472 (2019).
- 679 48. Allan Johnson, G. *et al.* Whole mouse brain connectomics. *Journal of Comparative Neurology* **527**, 2146–2157 (2019).
- 680 49. Yao, Z. *et al.* [A high-resolution transcriptomic and spatial atlas of cell types in the whole mouse brain](#). *Nature* **624**, 317–332 (2023).
- 681 50. Avants, B. B., Epstein, C. L., Grossman, M. & Gee, J. C. [Symmetric diffeomorphic image registration with cross-correlation: Evaluating automated labeling of elderly and neurodegenerative brain](#). *Med Image Anal* **12**, 26–41 (2008).

- 682 51. Tustison, N. J. *et al.* N4ITK: Improved N3 bias correction. *IEEE Trans Med Imaging* **29**, 1310–20 (2010).
- 683 52. Bajcsy, R. & Broit, C. Matching of deformed images. in *Sixth International Conference on Pattern Recognition (ICPR'82)* 351–353 (1982).
- 684 53. Bajcsy, R. & Kovacic, S. Multiresolution elastic matching. *Computer Vision, Graphics, and Image Processing* **46**, 1–21 (1989).
- 685 54. Gee, J. C., Reivich, M. & Bajcsy, R. Elastically deforming 3D atlas to match anatomical brain images. *J Comput Assist Tomogr* **17**, 225–36 (1993).
- 686 55. Klein, A. *et al.* Evaluation of 14 nonlinear deformation algorithms applied to human brain MRI registration. *Neuroimage* **46**, 786–802 (2009).
- 687 56. Murphy, K. *et al.* Evaluation of registration methods on thoracic CT: The EMPIRE10 challenge. *IEEE Trans Med Imaging* **30**, 1901–20 (2011).
- 688 57. Baheti, B. *et al.* The brain tumor sequence registration challenge: Establishing correspondence between pre-operative and follow-up MRI scans of diffuse glioma patients. (2021).
- 689 58. Avants, B. B. *et al.* The optimal template effect in hippocampus studies of diseased populations. *Neuroimage* **49**, 2457–66 (2010).
- 690 59. Avants, B. B., Tustison, N. J., Wu, J., Cook, P. A. & Gee, J. C. An open source multivariate framework for n-tissue segmentation with evaluation on public data. *Neuroinformatics* **9**, 381–400 (2011).
- 691 60. Manjón, J. V., Coupé, P., Martí-Bonmatí, L., Collins, D. L. & Robles, M. Adaptive non-local means denoising of MR images with spatially varying noise levels. *J Magn Reson Imaging* **31**, 192–203 (2010).
- 692 61. Wang, H. *et al.* Multi-atlas segmentation with joint label fusion. *IEEE Trans Pattern Anal Mach Intell* **35**, 611–23 (2013).
- 693 62. Tustison, N. J. *et al.* Optimal symmetric multimodal templates and concatenated random forests for supervised brain tumor segmentation (simplified) with ANTsR. *Neuroinformatics* (2014) doi:10.1007/s12021-014-9245-2.

- 694 63. Tustison, N. J., Yang, Y. & Salerno, M. [Advanced normalization tools for cardiac motion correction](#). in *Statistical atlases and computational models of the heart - imaging and modelling challenges* (eds. Camara, O. et al.) vol. 8896 3–12 (Springer International Publishing, 2015).
- 695 64. McCormick, M., Liu, X., Jomier, J., Marion, C. & Ibanez, L. [ITK: Enabling reproducible research and open science](#). *Front Neuroinform* **8**, 13 (2014).
- 696 65. Beg, M. F., Miller, M. I., Trouvé, A. & Younes, L. [Computing large deformation metric mappings via geodesic flows of diffeomorphisms](#). *International Journal of Computer Vision* **61**, 139–157 (2005).
- 697 66. Tustison, N. J. & Avants, B. B. [Explicit B-spline regularization in diffeomorphic image registration](#). *Front Neuroinform* **7**, 39 (2013).
- 698 67. Hsu, L.-M. *et al.* CAMRI mouse brain MRI data.
- 699 68. Reshetnikov, V. *et al.* High-resolution MRI data of brain C57BL/6 and BTBR mice in three different anatomical views.
- 700 69. Rahman, N., Xu, K., Budde, M. D., Brown, A. & Baron, C. A. [A longitudinal microstructural MRI dataset in healthy C57Bl/6 mice at 9.4 tesla](#). *Sci Data* **10**, 94 (2023).
- 701 70. Liu, J. *et al.* [Concordance of MERFISH spatial transcriptomics with bulk and single-cell RNA sequencing](#). *Life Sci Alliance* **6**, (2023).
- 702 71. Stringer, C., Wang, T., Michaelos, M. & Pachitariu, M. [Cellpose: A generalist algorithm for cellular segmentation](#). *Nat Methods* **18**, 100–106 (2021).
- 703 72. Jia, H., Yap, P.-T., Wu, G., Wang, Q. & Shen, D. Intermediate templates guided groupwise registration of diffusion tensor images. *NeuroImage* **54**, 928–939 (2011).
- 704 73. Tang, S., Fan, Y., Wu, G., Kim, M. & Shen, D. RABBIT: Rapid alignment of brains by building intermediate templates. *NeuroImage* **47**, 1277–1287 (2009).
- 705 74. Dewey, B. E., Carass, A., Blitz, A. M. & Prince, J. L. Efficient multi-atlas registration using an intermediate template image. in *Proceedings of SPIE—the international society for optical engineering* vol. 10137 (NIH Public Access, 2017).

- 706 75. Perens, J. *et al.* Multimodal 3D mouse brain atlas framework with the skull-derived coordinate system. *Neuroinformatics* **21**, 269–286 (2023).
- 707 76. Gong, H. *et al.* High-throughput dual-colour precision imaging for brain-wide connectome with cytoarchitectonic landmarks at the cellular level. *Nat Commun* **7**, 12142 (2016).
- 708 77. Wang, J. *et al.* Divergent projection patterns revealed by reconstruction of individual neurons in orbitofrontal cortex. *Neurosci Bull* **37**, 461–477 (2021).
- 709 78. Rotolo, T., Smallwood, P. M., Williams, J. & Nathans, J. Genetically-directed, cell type-specific sparse labeling for the analysis of neuronal morphology. *PLoS One* **3**, e4099 (2008).
- 710 79. Peng, H. *et al.* Morphological diversity of single neurons in molecularly defined cell types. *Nature* **598**, 174–181 (2021).
- 711 80. Kronman, F. A. *et al.* Developmental mouse brain common coordinate framework. *bioRxiv* (2023) doi:[10.1101/2023.09.14.557789](https://doi.org/10.1101/2023.09.14.557789).
- 712 81. Chon, U., Vanselow, D. J., Cheng, K. C. & Kim, Y. Enhanced and unified anatomical labeling for a common mouse brain atlas. *Nat Commun* **10**, 5067 (2019).
- 713 82. Tasic, B. *et al.* Adult mouse cortical cell taxonomy revealed by single cell transcriptomics. *Nat Neurosci* **19**, 335–46 (2016).
- 714 83. Bergmann, E., Gofman, X., Kavushansky, A. & Kahn, I. Individual variability in functional connectivity architecture of the mouse brain. *Commun Biol* **3**, 738 (2020).
- 715 84. Billot, B. *et al.* SynthSeg: Segmentation of brain MRI scans of any contrast and resolution without retraining. *Med Image Anal* **86**, 102789 (2023).
- 716 85. Tustison, N. J. & Amini, A. A. Biventricular myocardial strains via nonrigid registration of anatomical NURBS model [corrected]. *IEEE Trans Med Imaging* **25**, 94–112 (2006).
- 717 86. Avants, B. B. *et al.* The Insight ToolKit image registration framework. *Front Neuroinform* **8**, 44 (2014).
- 718 87. Falk, T. *et al.* U-net: Deep learning for cell counting, detection, and morphometry. *Nat Methods* **16**, 67–70 (2019).